Increased Speed: 3D silicon sensors; fast electronics – 1

***Abstract*—**Techniques to make fast, sub-nanosecond time resolution solid-state detector systems using sensors with 3D electrodes, current amplifiers, constant-fraction comparators or fast wave-form recorders, and some of the next steps to reach still faster results are described.

Index terms—solid-state detectors, silicon detectors, 3D sensors, short time resolution, fast pulses, speed.

I INTRODUCTION: A BRIEF HISTORY OF SHORT TIMES

Although reasonably fast readout electronics was available [1], in actual use, silicon radiation sensors, when originally introduced, were not particularly fast compared with contemporaneous detectors. For example, for the silicon detectors used in the pioneering UA2 experiment at CERN, "**the width of the shaped signal is 2 μs at half amplitude and 4 μs at the base**" [2]. Individual sensor elements were generally relatively large, and so had high capacitance while the charge from them, about 15,000 – 25,000 electrons and with no amplifying elements in the sensors, meant the voltage signals were small. So slow amplifiers, which integrated out a large part of the white noise generated at the input, were used.

The development of microstrip sensors [3] greatly reduced the capacitance between the top and bottom electrodes, adding a smaller, but significant one between adjacent strips. The custom, 128-channel, VLSI readout chip [4, 5], developed for those microstrip detectors and which made their use practical for collider vertex detectors, had amplifiers with 20 – 25 ns rise times, set by the need to roll off amplification below the frequency where one half cycle was equal to the round trip time for the signal to go through the inverter and be fed back to the input. (Otherwise the positive feedback would have produced a chip with 128 oscillators and no amplifiers.)

The planned use of microstrip detector arrays at colliders with short inter-collision times required a further increase in speed. Reference [6] describes a current amplifier with a rise-time of 4 ns and a pulse width at the base of 30 ns. All of these early amplifiers were developed to read out planar sensors.

Two developments now allow higher speeds in timing using silicon detector systems:

- Silicon sensors with 3D electrodes penetrating through the silicon bulk [7 – 27] allow charge from long tracks to be collected in a rapid, high-current burst. **Figure 1** shows a simplified view of such a sensor.
- Continued developments in integrated circuit technology fabrication permit the design and fabrication of even higher speed current amplifiers [28, 29, 30]. They can produce large voltage signals from those high speed input currents. Up to the sensor speed, such signals grow more rapidly than white noise with frequency.

But first, we examine some sources of timing errors.

II. TIMING ERRORS

Neglecting effects of radiation damage which will add additional items to the list below, the difference between the arrival time of an incoming particle and the value measured for that time can come from a number of sources.

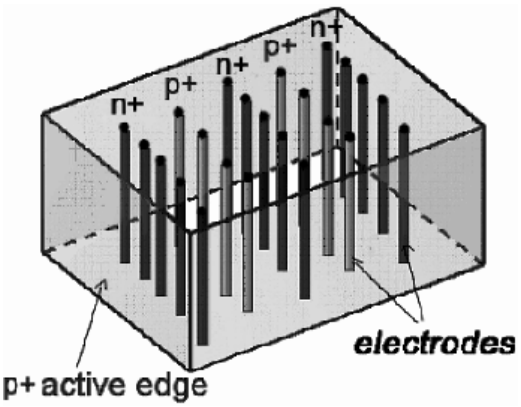

Figure 1. Schematic diagram of a 3D active-edge sensor.

1. **Variations in track location**
2. **Variations in track direction – 1 and 2** can affect the shape and timing of the detected pulse.
3. **Variations in total ionization signal –** Depending on the electronics, this can affect the trigger time.
4. **Variations in ionization location along the track – Delta rays** – high energy, but still generally non-relativistic, ionization ("knock-on") electrons. These tend to give an ever-larger signal when the Ramo weighting function [31 – 33] increases as they approach a planar detector electrode, with their current signal dropping to zero as they are collected. This produces a pulse with a leading edge that has changes of slope which vary from event to event, limiting the accuracy of getting a unique time from a specific signal amplitude for the track.
5. **Diffusion of charge carriers –** This causes spreading in space and time of a signal charge.
6. **Magnetic field effects affecting charge collection –** E × B forces may shift the collection paths.
7. **Measurement errors due to noise – This is currently the major error source.**
8. **Incomplete use of, or gathering of, available information** – This is a challenge mainly for the data acquisition electronics which, for high speed, will often have to face power and heat removal limitations. This topic is not covered in this paper.
9. In addition, long collection paths for thick planar sensors increase the time needed for readout and decrease the rate capabilities of the system.

A sensor with parallel 3D electrodes made from trenches filled with doped polycrystalline silicon separated by 0.1 mm, and described in section VI, can be made to be insensitive to the errors 1 – 7 above. In addition, one possible initial use would be timing of normally-incident particles with known locations and not in a magnetic field, making 1, 2 and 6 unimportant. In the barrel layers of detectors with solenoidal magnetic fields 3D sensors will have parallel E and B fields or with E × B in the direction of the track, producing no change in the collection path, so again 6 is unimportant.

However, additional discussion and calculations must be made for 3, 4, 5, and 7 – Landau fluctuations and the related delta rays, diffusion, and noise – to evaluate their effects.

III DELTA RAYS

To calculate the typical lateral delta range, we first calculate their production rate as a function of energy and initial angle [34], and then use *Casino V2.42*, a Monte Carlo program originally written for scanning electron microscopy, to see how the delta rays propagate [35].

1. Production rate. Charge z = 1 incident particles of mass M and momentum Mβγc will produce delta rays of kinetic energy T, where T is both much larger than the target ionization energy and much less than the maximum value of

$$T_{\max} = \frac{2m_e c^2 \beta^2 \gamma^2}{1 + 2\gamma m_e / M + (m_e / M)^2} \qquad (1)$$

at a rate given by:

$$\frac{d^2 n}{dTdx} = 2\pi N_A r_e^2 m_e c^2 \frac{Z}{A}\left(\frac{z}{\beta}\right)^2 \frac{F(T)}{T^2} \qquad (2)$$

N_A is Avogadro's number, r_e is the classical radius of the electron, Z/A for silicon is 0.498, z and β refer to the incident particle and usually equal 1, while the spin-dependent term F(T) is also close to 1 for most cases we will encounter. Integrating this from $T=T_1$ to T_2 (with $m_e c^2$ set at 511 KeV so all energies are in KeV) gives, for a silicon sensor thickness of s gm/cm^2,

$$n = 76.5s\int_{T_1}^{T_2} dT = 76.5s\left(\frac{1}{T_1} - \frac{1}{T_2}\right) \qquad (3)$$

The sensors used to collect the data of section VII were 170 μm thick, so we will use that as an example, and given $\rho_{Si} = 2.329$, we have

$$s = 0.0396 \text{ gm / cm}^2 \qquad (4)$$

and the number of delta rays with T between T_1 and T_2 is

$$n = 3.03(KeV)\left(\frac{1}{T_1} - \frac{1}{T_2}\right) \qquad (5)$$

For either incident multi-GeV pions or for 5 TeV protons (β≈1, $15 < \gamma < 5000$), T_{max} can range from several hundred MeV to close to 5 TeV. The total number of delta rays, is found by setting $T_2 = T_{max}$, a value far larger than the energies of the typical delta rays found in normal traversals, so the second term can be neglected. This gives a 10% probability for making a delta ray of 30 KeV or above.

The delta ray energy deposition will also depend on the location and thickness of material ahead of the sensor and of escape from the back side, but as will be seen, most delta rays have ranges small compared to the sensor thickness and so this will not be a large effect.

2. dE/dx It may be useful to compare these energies with

$$dE/dx_{min} = 1664 \text{ KeV per gm / cm}^2 \text{ for silicon,}$$

which will give a mean total energy loss of

$$\Delta T = 2.329 \text{ x } 0.017 \text{ x } 1664 = 65.88 \text{ KeV,}$$

using the thickness of the sensors that gave the data shown in the last part of this paper.

3. Production angle, θ: The production angle can be found for an electron of kinetic energy T, and corresponding momentum p, maximum momentum p_{max} and maximum kinetic energy T_{max} from:

$$\cos\theta = \left(\frac{T}{p}\right)\left(\frac{p_{max}}{T_{max}}\right) \qquad (6)$$

Cos θ is close to 1 (forward) for relativistic (large γ) delta rays since both T/pc terms are close to 1:

$$\frac{p_{max}c}{T_{max}} = \frac{\beta\gamma mc^2}{(\gamma-1)mc^2} = \frac{\beta\gamma}{(\gamma-1)} = \frac{\left(1-1/\gamma^2\right)^{1/2}\gamma}{\gamma-1} = \frac{\left(\gamma^2-1\right)^{1/2}}{\gamma-1} = \left(\frac{\gamma+1}{\gamma-1}\right)^{1/2} \approx 1 \qquad (7)$$

However, for low kinetic energy (γ « 1),

$$T/pc = (\tfrac{1}{2}\, mv^2) / mvc = v / 2c \approx 0 \qquad (8)$$

The cos θ term is the product of a term near one and another near zero, so the production angle is large. Specifically, starting with the very probable **T = 3 KeV**, and continuing with the increasingly less probable **T = 10, 30, and 60 KeV**, the angles are **86°, 84°, 80°, and 76°.**

4. Range: At the energies common in silicon sensors, virtually all the delta ray tracks scatter to large angles. Typical paths and energy deposition for them given by *Casino* are shown in **Figures 2 – 7**. As can be seen in **Figure 2**, the common 3 KeV delta rays, with typical ranges of 0.1 μm leave their ionization so close to the track that they do not influence the timing for tracks parallel to the electrodes of 3D sensors.

10 KeV delta rays (see **Figure 3**) have typical ranges of 0.5 μm, and will be oriented to lead the rest of the track about ¼ of the 30% of the time they or higher energy delta rays are present. With typical electron drift velocities of about 5 x 10^6 cm / sec, the leading edge of the delta ray could reach an n electrode up to 10 ps ahead of the main track, and could slightly affect the timing. But with typical deposition energies for the entire track of 60 – 80 KeV (see section 2 above) and typical signal-to-noise ratios of 15 to 1 or

better, 10 KeV is at the start of the range where the presence of such delta rays should be identifiable.

A multiple-plane detector then would not only provide improved statistical accuracy, but could alter the weighting of the 5 – 10% of events with high-energy delta rays. The most accurate detectors – ones using fast waveform recorders – could discard data from tracks made near collecting electrodes. The other delta ray events, with extra ionization, and so increased signal to noise ratio will give the most accurate results as noise is, at the present time, the most important source of error. This will be covered in section VIII.

Continuing up the energy scale, 30 KeV delta rays (see **Figure 4**) have typical ranges of several microns and would affect timing, but can be identified by the large increase in pulse height, which will place them in the Landau tail.

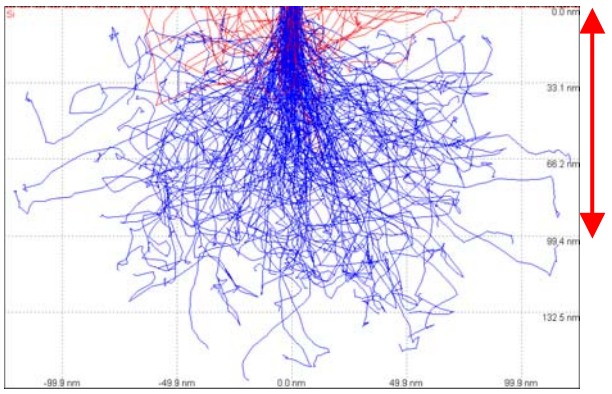

Figure 2. 200 3-KeV delta rays. Red lines trace paths of backscattered tracks. The arrow is 0.1 µm long.

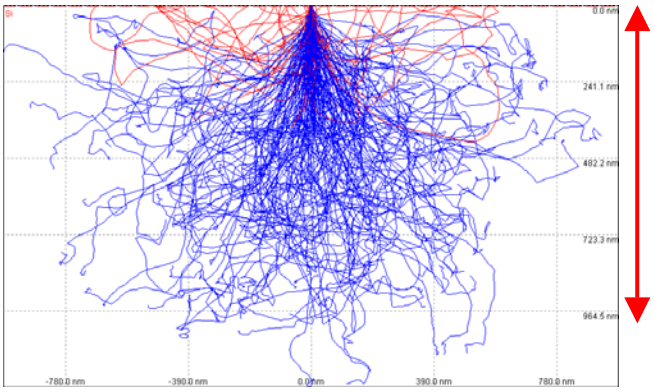

Figure 3. 200 10-KeV delta rays. Red lines trace paths of backscattered tracks. The arrow is 1 µm long.

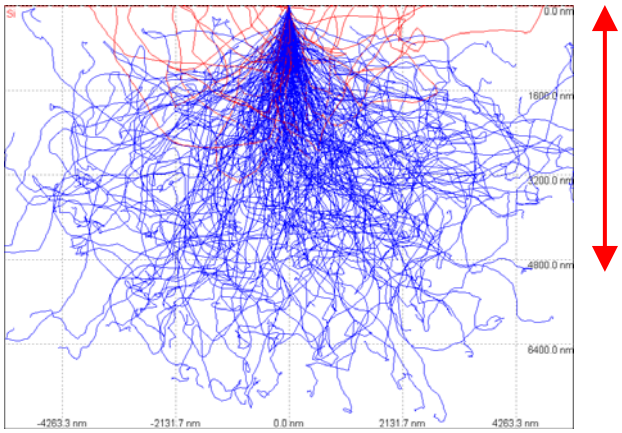

Figure 4. 200 30-KeV delta rays. Red lines trace paths of backscattered tracks. The arrow is 5 µm long.

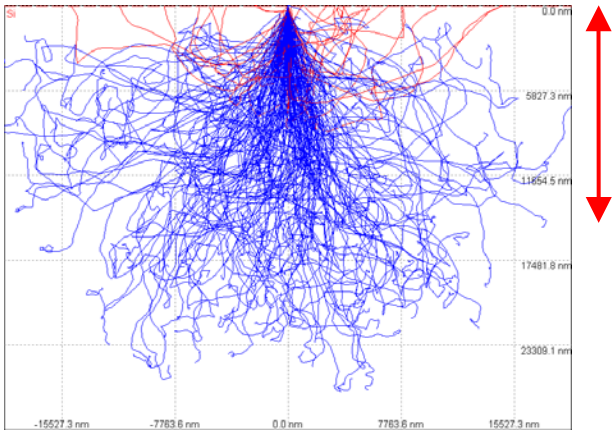

Figure 5. 200 60-KeV delta rays. Red lines trace paths of backscattered tracks. The arrow is 15 µm long.

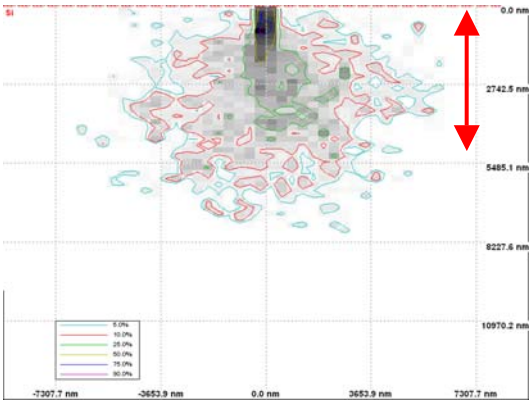

Figure 6. 200 30-KeV delta rays, energy deposition. The 50% containment contour goes to a depth of 2.0 µm with a maximum full width of 0.8 µm. The 75% contour goes to a depth of 4.3 µm with a maximum full width of 2.7 µm. The arrow is 5 µm long.

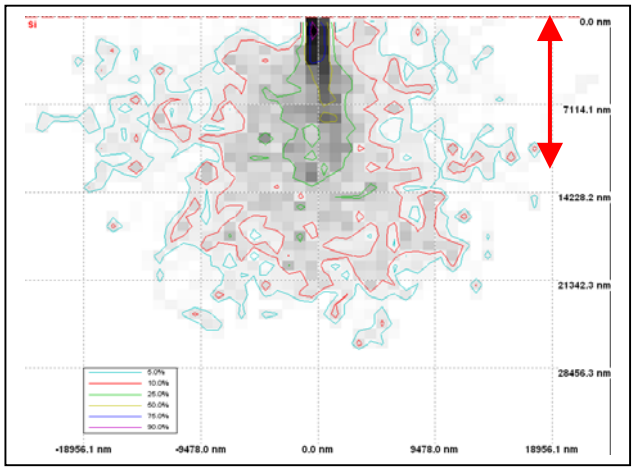

Figure 7. 200 60-KeV delta rays, energy deposition. The 50% containment contour goes to a depth of 8.0 µm with a maximum full width of 2.0 µm. The 75% contour goes to a depth of 13.5 µm with a maximum full width of 7.3 µm. The arrow is 15 µm long.

IV DIFFUSION

As any charge travels to an electrode, it diffuses around the point on the path it would otherwise follow having a Gaussian distribution with

$$\sigma = \sqrt{2Dt} = \sqrt{2D\frac{s}{v}} \qquad (9)$$

where D is the diffusion constant, often given as 35 cm^2/s for electrons and 12 cm^2/s for holes, and s is the drift distance and v the velocity. This will cause a spread in arrival times of

$$\sigma_t = \sqrt{2D\frac{s}{v^3}} \qquad (10)$$

However, D can vary, depending on the value of the electric field, **E**, the temperature, the direction – parallel or perpendicular – to **E**, and to a small extent, neglected here, to the direction of the crystal axis [36, 37].

V. SPEED AND TRIGGERS FROM RANDOM NOISE

It is often assumed that limiting the band width will reduce noise, and so reduce false triggers from noise. However, the fast intrinsic pulse times, τ_{det}, can, with well-designed current amplifiers, produce high signal-to-noise ratios, as the signal current is proportional to the detector speed while, for instance, noise across a resistance such as a transistor channel only grows as the square root of the frequency spread. **So increasing the speed of an amplifier up to the highest predominant speeds of the sensor can then improve the performance of a current-amplifier based circuit.**

One example, useful for studying the rate of false noise triggers, is the number of traversals per second, n, of a Gaussian noise current I_n with a positive slope past a threshold level [38] as sketched in **Figure 8.**

$$n = \left[\frac{\int_0^\infty \nu^2 p(\nu) d\nu}{\int_0^\infty p(\nu) d\nu} \right]^{0.5} \exp\left(\frac{-I_t^2}{2\overline{I_n^2}} \right)$$

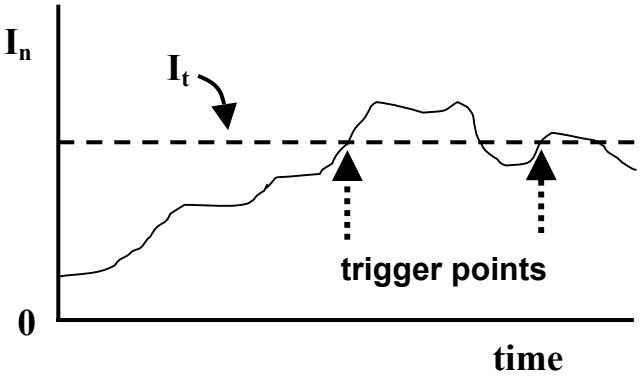

Figure 8. Sketch of a pulse and its trigger points

For a filter, p(ν) dν , that is flat from ν1 to ν2, and with (typically) ν2 >> ν1, we have:

$$n = \left[\frac{\nu_2^3 - \nu_1^3}{3(\nu_2 - \nu_1)} \right]^{1/2} \exp\left(\frac{-I_t^2}{2\overline{I_n^2}} \right) = \frac{\nu_2}{\sqrt{3}} \exp\left(\frac{-I_t^2}{2\overline{I_n^2}} \right)$$

I_t can be set equal to a fraction a_1 of $\overline{I_{det}}$, the average value of the signal pulse current.

$$I_t^2 = a_1^2 \, \overline{I_{det}}^2 = a_1^2 \langle q./\tau_{det} \rangle^2 = a_2 \, \nu_{det}^2$$

Here q is the total charge, τ_{det} is the pulse duration, and $\nu_{det \text{ is } 1/\tau_{det}}$. The constants a_1 and a_2 are independent, to first order, of ν. White noise currents in electronics capable of matching detector speeds will have $\nu_h \approx \nu_{det}$ and

$$\overline{I_n^2} = a_3 \Delta\nu = a_3(\nu_h - \nu_l) \approx a_3 \nu_h = a_4 \nu_{det}$$

(For a resistor, a_3 would equal 4KT/R.) The threshold level squared can be increased in proportion to the detector speed squared, giving a near-exponential drop in noise counts that is proportional to the detector speed.

$$n = \left(\frac{\nu_{det}}{\sqrt{3}} \right) \exp\left(-\frac{a_2 \nu_{det}^2}{2 a_4 \nu_{det}} \right) = \left(\frac{\nu_{det}}{\sqrt{3}} \right) \exp(-a_5 \nu_{det})$$

A simple integrator will not benefit from this speed. The circuit must respond only to rapid changes in voltage on an integrating capacitor or to high instantaneous currents in a resistive circuit.

VI REDUCING TIMING ERRORS

At some level, systems can be chosen that will permit corrections to the effects listed above. **Multiple layers** can provide the track information for **1**, **2, 3** and **7** in Section II

and increased statistics to make **6** less important**. Low temperatures** will decrease noise and increase circuit speeds.

For several reasons, **3D sensor** signals can be intrinsically faster than planar ones:

- The 3D electrode spacing can be less than the wafer thickness, so carrier drift distances are shorter.
- Depletion voltages are low so the use of over-voltage means that collection fields can be more uniform and uniformly high.
- In addition, in 3D, the field lines end on surfaces which normally have more area than corresponding planar electrodes, so the ratio of the average drift fields to the peak field can be larger for 3D sensors. (There is a price for this: increased electrode capacitance.)
- Delta-ray ionization along the track arrives sequentially in planar sensors, adding slope changes to the pulse, while for tracks parallel to 3D electrodes, arrives nearly simultaneously, modified mainly by the delta ray ranges and by diffusion of the ionization (about 1 μm in the first ns and growing as the square root of time).
- These delta rays arrive late. Normally this part of the pulse would not be used in timing as the shape varies when either the electron or hole collection ends.
- Common, low energy delta rays, with a range short compared to the gap, are collected within a few picoseconds. Higher energy ones are rare and recognizable.
- Both types of 3D electrodes can be contacted on a single surface, so if capacitative readout for at least one type of electrode can be used, recording pulses from both the n^+ and p^+ electrodes may improve both time and spatial resolution. The same charge signal goes to spatially separated electrodes, providing additional track information and can improve the signal to noise ratio, giving better timing.
- Solenoidal magnetic fields in 3D barrel-layer (but not end-cap) sensors at most just shift the ionization column along its own length and to first order, have no effect on timing.

Trench (or "wall") electrodes (**See Figures 9 and 10**) provide additional advantages, particularly for tracks that are not close to electrodes or their subdivisions. A section having two facing 100 μm gaps with a common electrode and a 250 μm thickness (in the track direction) will have a capacitance of 0.527 Pf per mm of width.

- There are no repeating null-field points.
- They have a particularly high average field / peak field ratio.
- Far enough away from pixel boundaries, the Ramo weighting field will be constant.
- Larger gaps will lower the capacitance, improving the signal-to-noise ratio, and reduce the fraction of tracks crossing close to an electrode where analysis is more difficult. But they will require higher bias voltages and will have a longer clearing time.

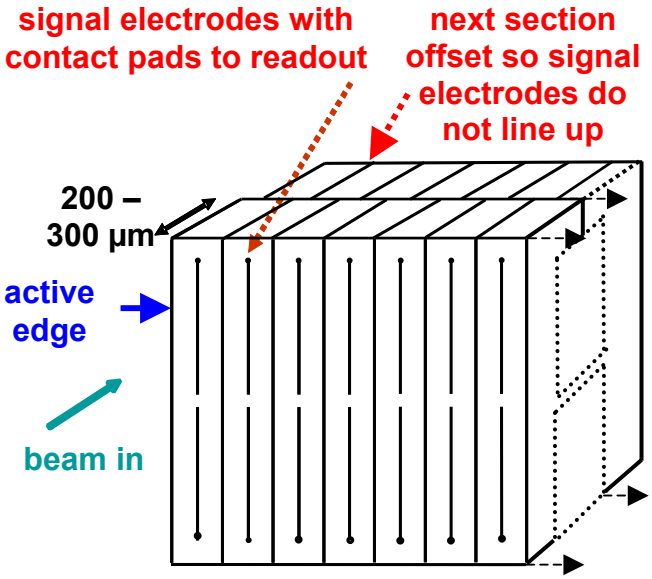

Figure 9. Schematic diagram of part of one section of two of the planes in an active-edge 3D trench-electrode detector. Other offsets (⅓, ⅔, 0, ⅓, ⅔ ..etc.) may also be used.

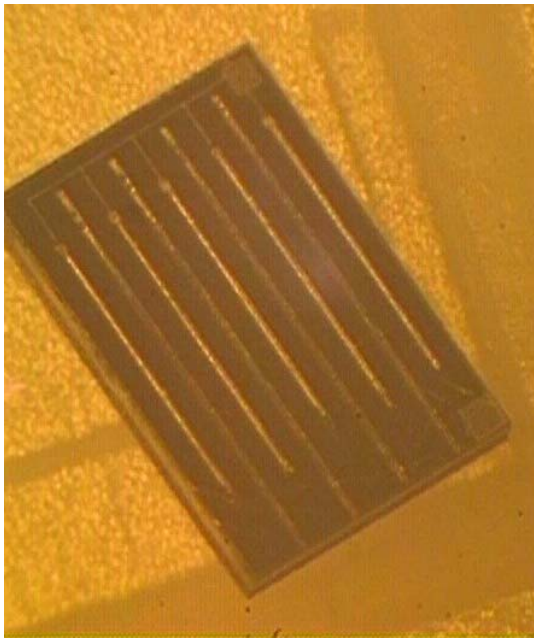

Figure 10. 3D trench-electrode sensor.

- If the bias electrodes are also instrumented, they will have the same magnitude, but opposite sense, current signal. The bias electrodes can then have pixel boundaries at the mid-points of the signal electrodes, roughly doubling the spatial resolution in the vertical direction in **Figure 9**, and always providing a constant Ramo field on at least one electrode plane.

- For moderate to high bias voltage levels (~ 50 V) and low dopant levels (~ 5 x 10^{11} / cm^3) the depletion voltage of ~ 2 V will introduce only a small change in the constant charge-carrier drift velocity. After irradiation, the electric field will not be uniform, but the velocity will be faster as the bias voltage can normally be raised, and at high-field values and velocity saturation, will again be nearly constant.

- The wall-to-wall pitch will normally be large compared to most all delta ray lateral ranges, so the ionization columns will move without shape changes, other than those due to diffusion, for all but a small subset of tracks crossing close to an electrode.

- There will be a varying delay, normally under a picosecond, given that the index of refraction of silicon is only 3.95, for the electromagnetic pulse from the separating holes and electrons to travel to the electrodes.

- **Beyond that delay, the time, shape, and magnitude of the leading edge of the pulse will depend mainly on the time of the track traversal, on the local drift velocity, and on the track location for tracks near pixel boundaries. Figure 11** shows an idealized diagram of this expected induced current shape.

- **With a known sensor signal input shape for tracks that are distant from pixel boundaries, use of a waveform recorder as an electronics input device – if they**

can be made to fit in the area of one pixel – would provide a powerful tool. The time delay so this most closely matches the experimental waveform would provide a time measurement with reduced sensitivity to small-scale noise fluctuations.

- **The dominant remaining source of error is noise. The next section describes example of the improvement from the use of a waveform tracer and sample measurements of the size of this source of error.**

	electrons		holes		units
temperature	293.15	245	293.15	245	°K
v_m	10.92	12.85	8.446	9.308	10^6 cm/s
E_c	6734.6	5040.0	17303	12638	V/cm
β	1.9197	0.9652	1.2083	1.1705	
V_d (E = 0.2 V / μm)	2.6143	4.0	0.92035	1.41	10^6 cm/s
V_d (E = 0.5 V / μm)	4.9286	7.0	2.0657	2.22	10^6 cm/s
V_d (E = 1.0 V / μm)	6.9072	8.8	3.4598	4.62	10^6 cm/s
$D_{parallel}$, 0.2 V / μm)	32		12.3		cm^2 / s
$D_{parallel}$, 0.5 V / μm)	21		10.7		cm^2 / s
$D_{parallel}$, 1.0 V / μm)	13.5		7.36		cm^2 / s
t (E = 0.2 V / μm)	3.83	2.83	10.9	7.57	ns
$\sigma_{t,\ parallel\ diffusion}$	0.19		0.56		ns
t (E = 0.5 V / μm)	2.03	1.61	4.84	3.53	ns
$\sigma_{t,\ parallel\ diffusion}$	0.059		0.16		ns
t (E = 1.0 V / μm)	1.45	1.21	2.89	2.22	ns
$\sigma_{t,\ parallel\ diffusion}$	0.029		0.06		ns
max δ-ray collection times					
3 KeV (1 V / μm)	1.9	1.5	3.8	2.8	ps
10 KeV (1 V / μm)	14	11	29	22	ps
30 KeV (1 V / μm)	101	80	202	152	ps
60 KeV (1 V / μm)	362	284	723	541	ps

Table 1. Velocities, diffusion, and collection times for a 0.1 mm parallel-plate trench electrode gap.

Table 1 gives the maximum electron and hole drift times for the 0.1 mm gap for tracks near one or the other trench electrode. It also gives the room temperature arrival time spread caused by diffusion – about 2% to 5% of the corresponding drift times. Even this

small value should not significantly increase timing errors, as unlike delta rays, which may or may not be present, the particle statistics shaping this leading edge are high.

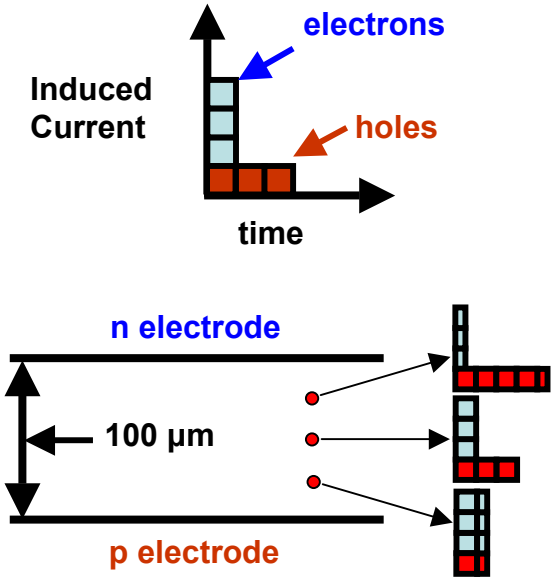

Figure 11. Schematic diagram of induced currents from a track in a parallel-plate trench-electrode sensor. It is assumed the track is parallel to the plates, and the electron and hole drift velocities are constant with a 3 to 1 ratio. The plane of the bottom diagram is perpendicular to the track and ion columns.

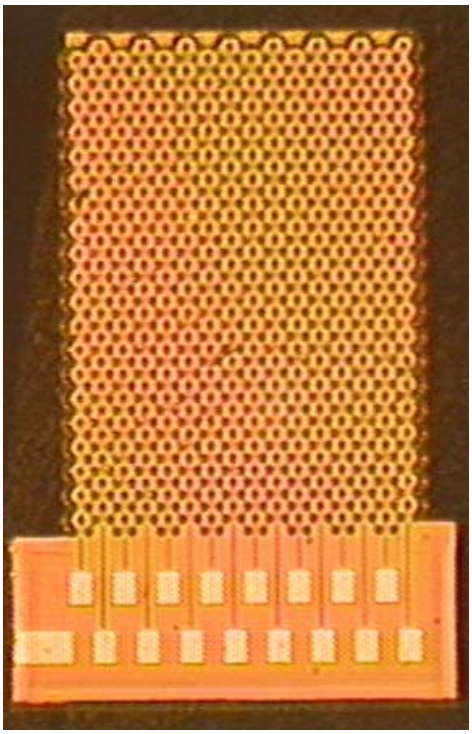

Figure 12. 3D hexagon-cell active edge sensor tiled with 16 columns, each with 20 hexagons with sides of 50 µm connected to the 16 pads at the bottom.

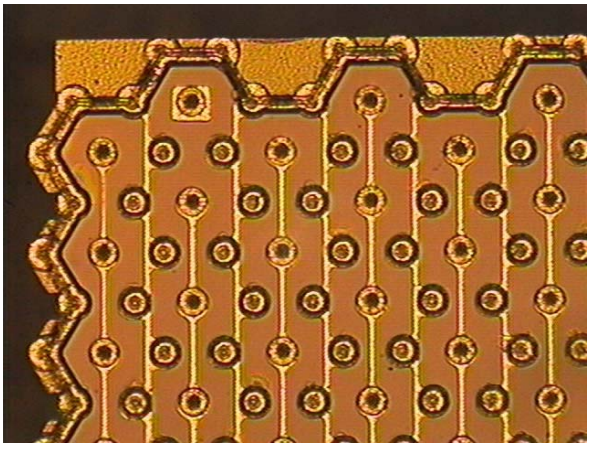

Figure 13. Magnified view of the top corner of the hexagon sensor.

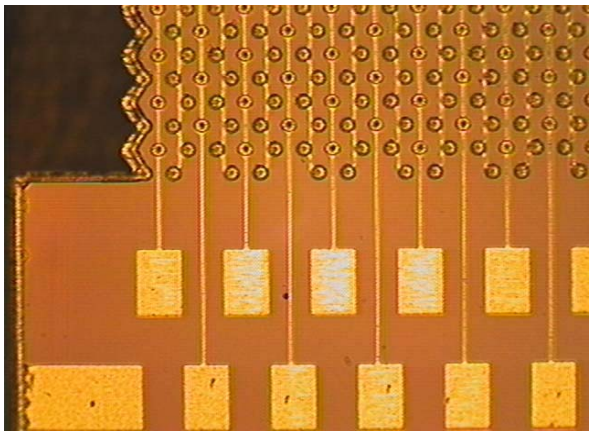

Figure 14. Output pad end of 3D active-edge hexagon sensor.

VII NOISE AND TIME RESOLUTION

We did not have a large enough trench-electrode sensor for use with our ^{90}Sr beta source, so have started with a 170-micron thick 3D active-edge sensor having:

- hexagonal cells with each hexagon side 50 μm in length,
- with 20V bias at room temperature,
- arranged with 16 sets of 20 hexagons with ganged central electrodes,
- with each of the 16 columns going to one channel of a fast 0.13μm-technology VLSI current-amplifier chip developed by M. Despiesse, G. Anelli, P. Jarron, et al.
- exposed to un-collimated ^{90}Sr betas. Three adjacent channels were sent to
- an Agilent 54832B 1 GHz oscilloscope which displayed each at 16 x 10^9 8-bit samples per second, with
- the oscilloscope triggered by the signal on the central channel.

Figure 12 shows a view of the entire sensor. **Figure 13** shows a corner and end of one sensor away from the wire bond end, and **Figure 14** shows some of the wire bond pads along the bottom. One hundred events were taken, with one being inadvertently stored twice, providing 99 for study. Each event stored 3 x 800 3-digit pulse heights separated by 62.5 ps, so covering a time-span of 50ns.

For several reasons, this sensor will not provide the fastest available speeds:

- With 20 ganged cells, the capacitance is on the high side by pixel standards.
- The bias voltage used was well below the maximum possible.
- The operating temperature, 20°C, is higher than the expected -20°C or lower for operation at the LHC, resulting in lower drift velocities and a slower readout circuit.

In addition, angled tracks that stayed in one channel's electrodes and did not deposit ionization in the two adjacent channels may have a different collection-time behavior from that of normally-incident beam particles.

Figures 15 and 16 show typical events with pulses in more than one channel. 67 events had a pulse in only one channel. One of them, the 50th to trigger, with a normal shape, had a second pulse in a neighboring channel, but delayed by 4 ns and with a shape that differs from that of the other events. It may have been a combination of noise and the induced signal seen on the green trace in **Figure 17**. The first, middle, and last of the 67 events are shown in **Figures 17, 18, and 19.**

Figure 20 shows the event with the lowest pulse height of the 67.

The noise was measured from the differences between each of the leading 270 points and the 270-point base line average for the time before each of the 67 pulses. **Figures 21** (linear scale for best view of the peak) and **22** (logarithmic, with doubled bin size to improve statistics, for the tails) show the distribution which is Gaussian with no visible tails. The σ_{noise} for the linear plot is 0.332 mV, for the log plot is 0.333 mV, and for the 67 x 270 = 18,090 points directly, is 0.322 mV. Changing the bin size to 0.05 mV in the

log plot (not shown) changes the σ from 0.333 mV to 0.322 mV. The differences between these values are small and within the expected statistical errors. The distribution of these base line averages is shown in **Figure 23.**

While Gaussian, the noise is not white, due to frequency limitations of the amplifier. The Fourier transform of the noise is shown in **Figure 24**. The distribution peaks at 62.5 MHz, drops to 30% of the peak at 200 MHz and to nearly to zero at 600 MHz, corresponding to cycle times of 16 ns, 5 ns, and 1.6 ns. These are comparable to time durations for base line full-widths of the 3D sensors: 5 – 9 ns. Both are limited by the frequency response of the amplifier although the noise does have some low-amplitude pulses of somewhat higher frequency.

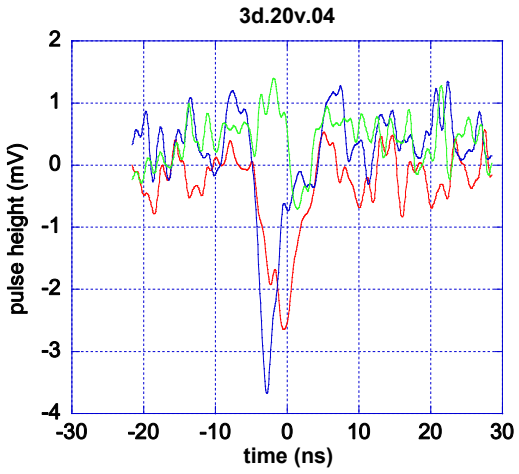

Figure 15. A track in the trigger (red trace) column and one neighboring column (blue trace) of sensors and an induced pulse (green) in the other adjacent neighbor.

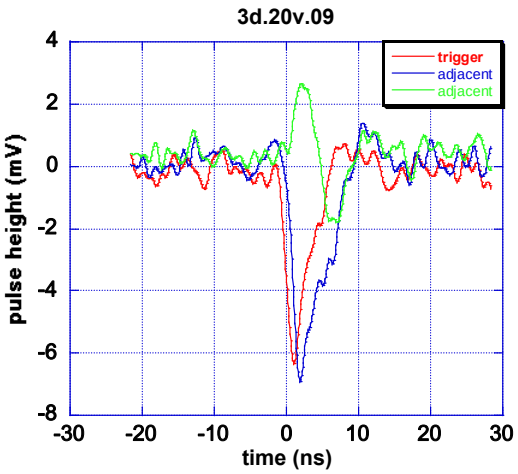

Figure 16. A second event with tracks in two adjacent columns of pixels. The data for all figures were taken at 20° C. The underlying points in all traces were separated by 62.5 ps.

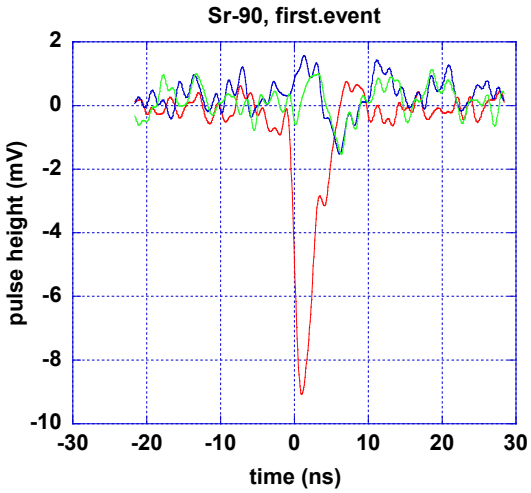

Figure 17. The first of 67 single-channel events (of 99 total triggers).

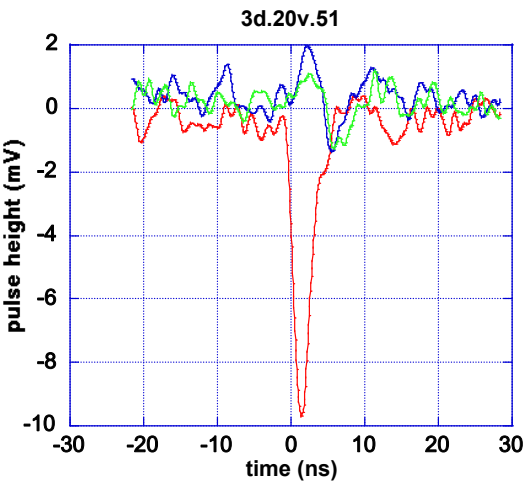

Figure 18. The middle event.

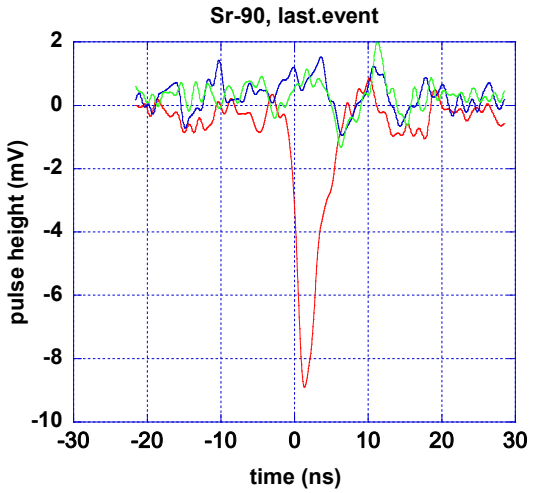

Figure 19. Event 99, the last event.

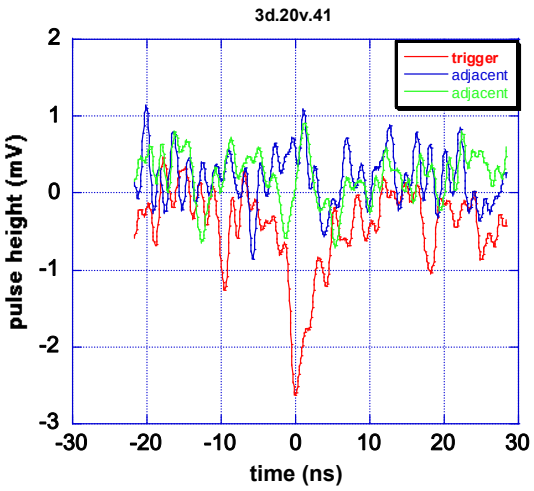

Figure 20. The single-column event with the lowest peak amplitude.

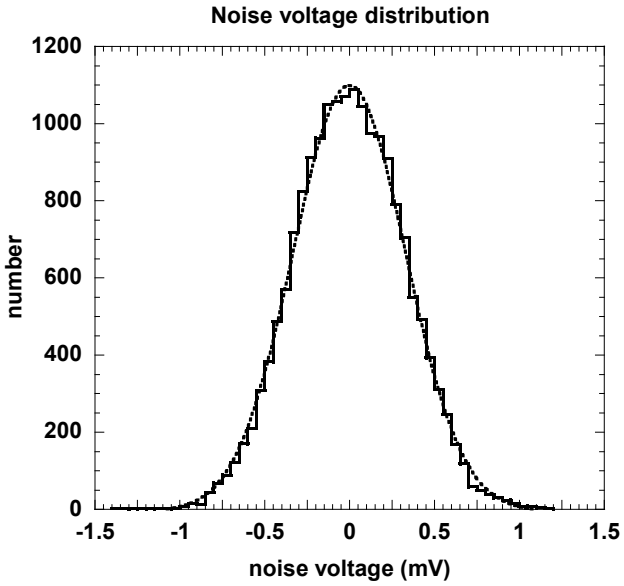

Figure 21. Sum distribution for all 67 events of the 270 base line noise points prior to each of the Sr-90 pulses relative to the average value of those 270 points. The σ of the distribution is 0.332 mV.

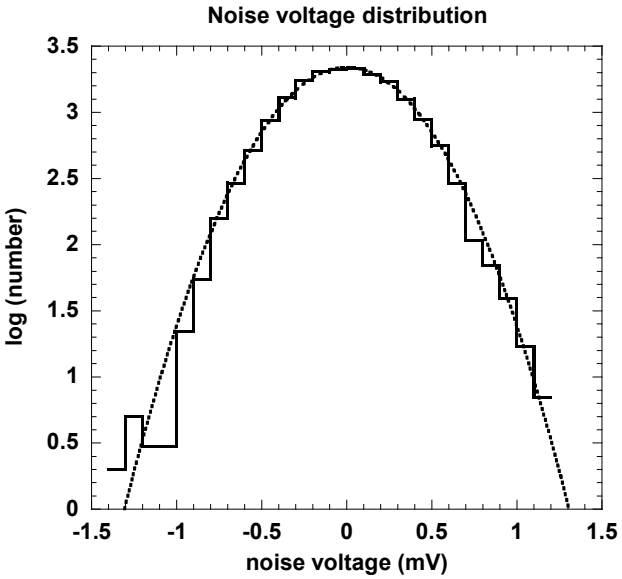

Figure 22. Log sum distribution for the same noise points. The σ of the distribution is 0.333 mV. The bin widths are doubled to better show the fit of the tail statistics.

We can now calculate the expected noise-induced error:

1. remove events with pulses in either of the neighboring channels
2. average the first 270 points to find the base line level
3. find the peak height (with our negative pulses, the lowest value)
4. find the points closest to 50%, where the slope is greatest, and from them

5. calculate the slope, $s = \{V(t_+) - V(t_-)\} / (t_+ - t_-)$
6. calculate the noise-induced expected timing error $dt = \sigma_{noise} / s$.

Figure 25 shows a scatter plot of σ_{noise} vs. pulse height and on the top and right-side axes, the projected distributions of each. The median and average dt values are 129 and 155 ps and, as expected, there is a clear pulse-height dependence.

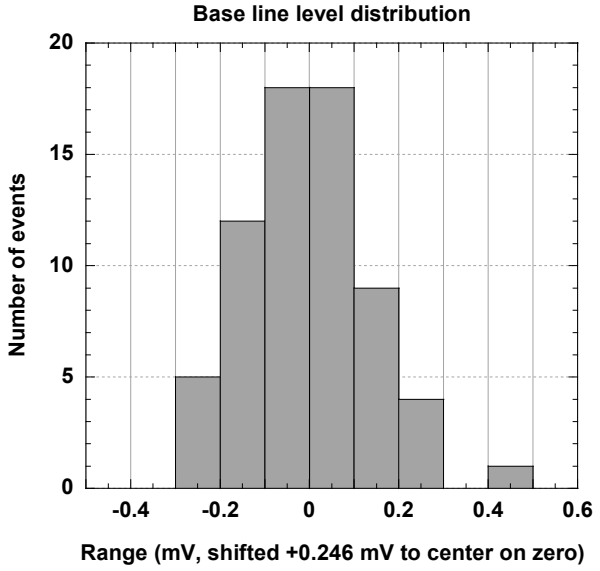

Figure 23. Base line event-to-event shift distribution. The standard deviation of the 67 events is 0.14 mV.

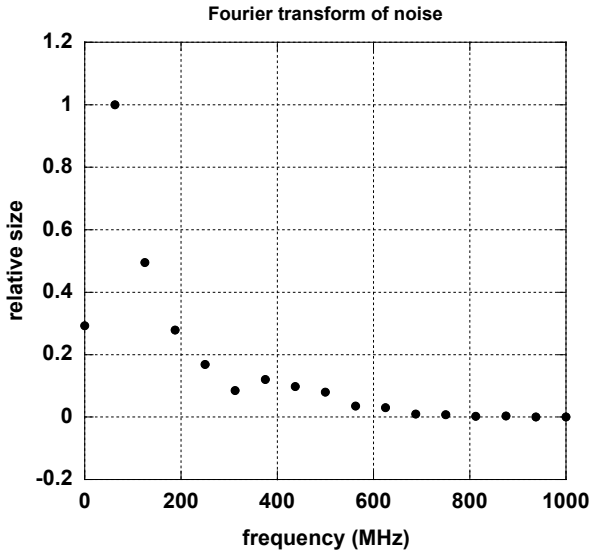

Figure 24. Fourier transform of the noise.

VIII THE WORST PULSE AND WHAT TO DO ABOUT IT

Figure 26 shows the pulse with the largest expected timing error. The pulse is small, and the phase of the noise has reduced the slope at the 50% point used here to simulate a constant fraction discriminator set for what is normally the steepest part of the rise. In addition, the limited frequency ranges of both the noise and signal suggest the possibility of a correlated effect where the noise, for example, increases the peak pulse height and also partially increases the pulse amplitude at the 50% point, decreasing the error. A different phase could increase the error beyond the value calculated in 1-6 above.

To investigate these possibilities and test a method less sensitive to such effects, two additional methods were tried, both of which used data to provide almost pure noise and almost pure noise-free pulses. Steps 1 – 5 are the same for both.

1. An approximately noise-free signal pulse shape was found by adding the six pulses above 10 mV, which are already relatively noise-free. To allow for the slight trigger-time variations, the individual curves were shifted by amounts of up to ± 0.25 ns to align the peaks. The noise, being random, tended to cancel as can be seen in **Figure 27**, showing the entire sum pulse and **Figure 28**, showing with

an expanded scale, the leading edge. This cancellation can also be seen in **Figure 29,** which shows a pulse from a pulse generator set to have a rise time of 800 ps, and also the sum of 5 such pulses.

2. A set of noise sequences was prepared by subtracting the average of each 270-point pre-pulse base line from the 270 points to remove common-mode signals from each of the 67 traces.
3. The 67 baselines were subdivided into 67 x 3 = 201 sets of 90 points each, covering (90 / 16) ns, a time longer than the pulse-sections used (the rise once above the noise-level, the top, and the first part of the trailing edge.)
4. The stored signal pulse amplitudes were multiplied by a fraction to reduce them to the average height of groups of the 67 signals, from the 6 in the smallest pulse height group (2.7483 mV for 2.58 to 2.99 mV), …(3.8517 mV for the 6 from 3.64 to 4.03 mV) and with smaller-sized groups in the Landau tail up to the largest signal, 14.9 mV.
5. The first noise sequence was added, point-by-point, to each signal.
6. Interpolating, the time of the 50% level-crossing was found for each.
7. This was repeated for the rest of the 67 x 3 noise sets for all signal heights.
8. The dt_{noise} for each signal size was found from the rms variation about the mean of the 201 50% crossing times and is given in **Figure 30**.

This method will be sensitive to the sort of random noise fluctuations seen in **Figure 26**. Finally a pulse fitting method was used. This avoided use of low-level parts of the signals where noise was most important, and of signals toward the end where the hole-collection bulge could cause variation. So the digital pulse shape that was added to the repeated noise sequences ran from data point 10 (0.5625 ns) to 76 (4.6875 ns) and the fitted function, which was going to be shifted back and forth in steps of 62.5 ps to find the best fit ran from points 20 to 61. In detail:

6. The peak of the digital pulse **plus noise** in step 5 above was used to adjust the peak height of the pulse to be fitted, and proportionately, all of the other points. So all of these points will be off by a common but realistic error factor. Since the same function is used for both pulses, errors from track angle variations will not be present, but they will also not be present in the first likely use which will employ high-energy, normal tracks.
7. The fitted track amplitudes were subtracted, point-by-point from the signal plus noise.
8. The standard deviation of these differences was calculated.
9. Steps 7 and 8 were repeated with the fitted set shifted one point (62.5 ps) later.
10. Steps 7–9 were repeated with the 20-61 fit range shifted from one end of the underlying signal plus noise range 10-76 to the other, for a total of 26 trial fits..
11. The minimum standard deviation of the 26 was found.

12. A parabola was fit to that minimum value and the two values on each side. The minimum location will be used to interpolate between the steps. A parabola with (x,y) points -x, 0, x and y_1, y_2, y_3 (x = 62.5 ps) has a minimum at:

$$; \qquad x_0 = (x / 2)(y_1 - y_3) / (y_1 - 2\, y_2 + y_3)$$

14. The standard deviation of these 201 interpolated parabola minima was found and is plotted in **Figure 30**.

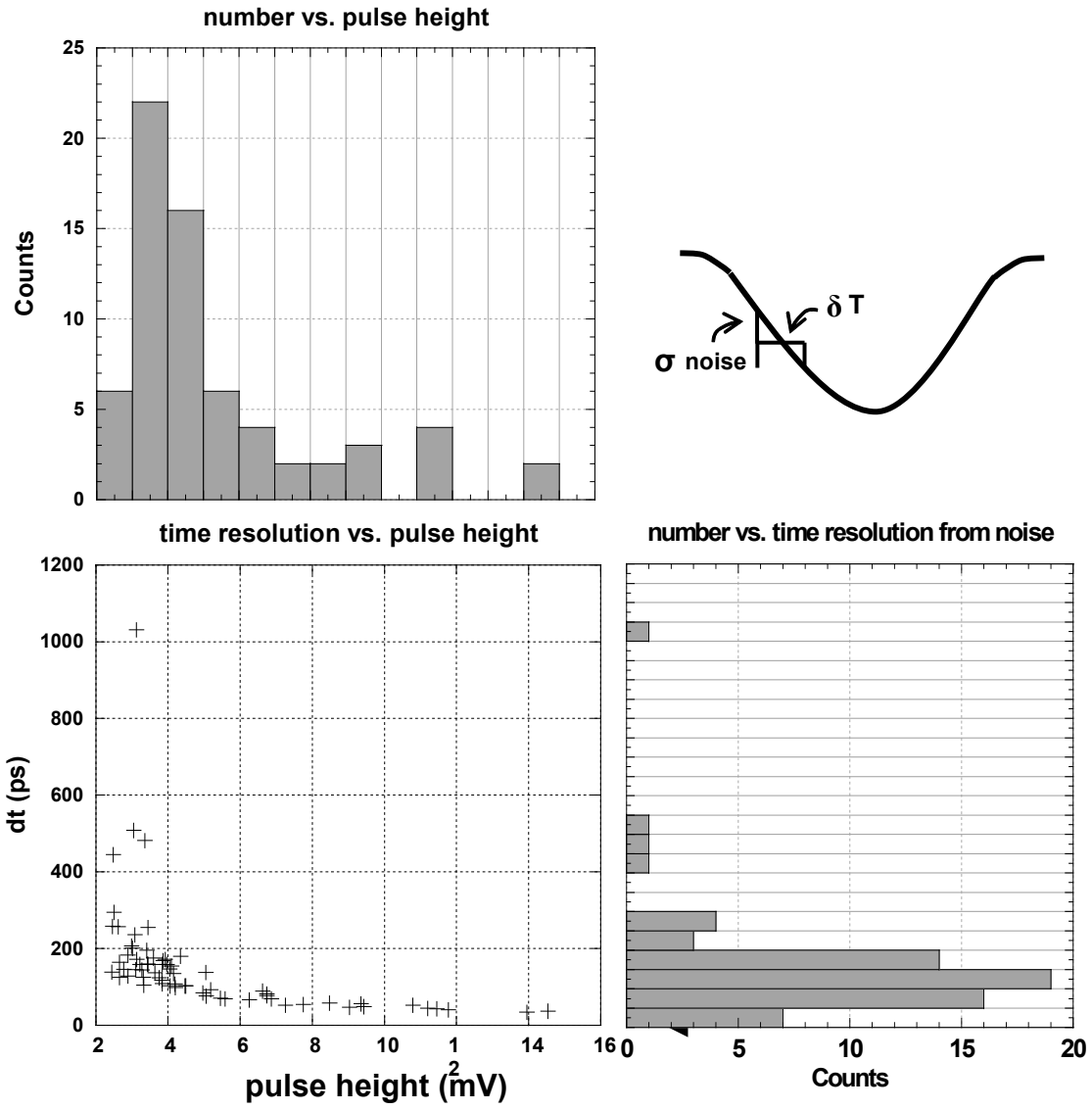

Figure 25. Noise induced time errors, dt, vs. pulse heights, V, for 67 pulses and the projections of the dt and V distributions. The relationship is shown in the upper right diagram. The signal to noise ratio is 3 times the pulse height in mV.

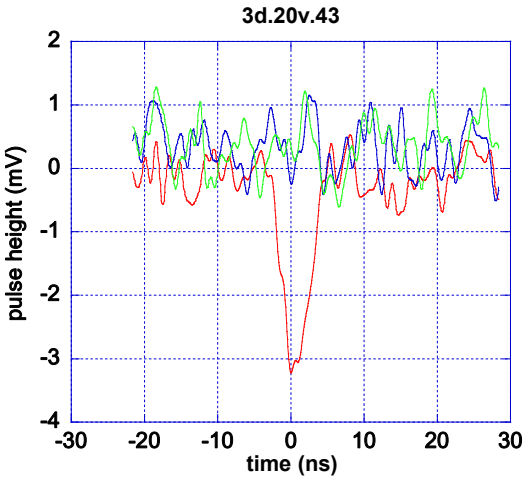

Figure 26. The single-column event with the largest expected timing error in the central scatter plot of Figure 25.

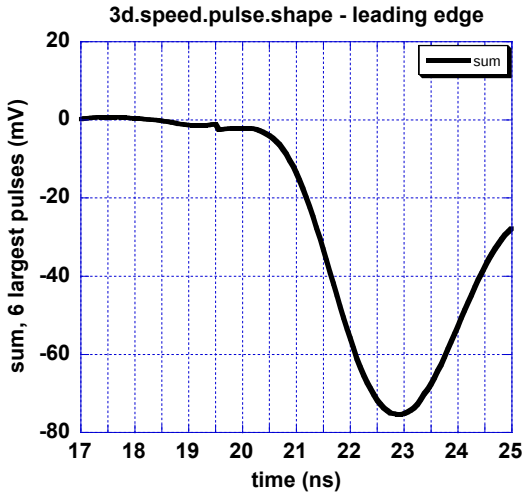

Figure 28. The leading edge of the pulse in Figure 27.

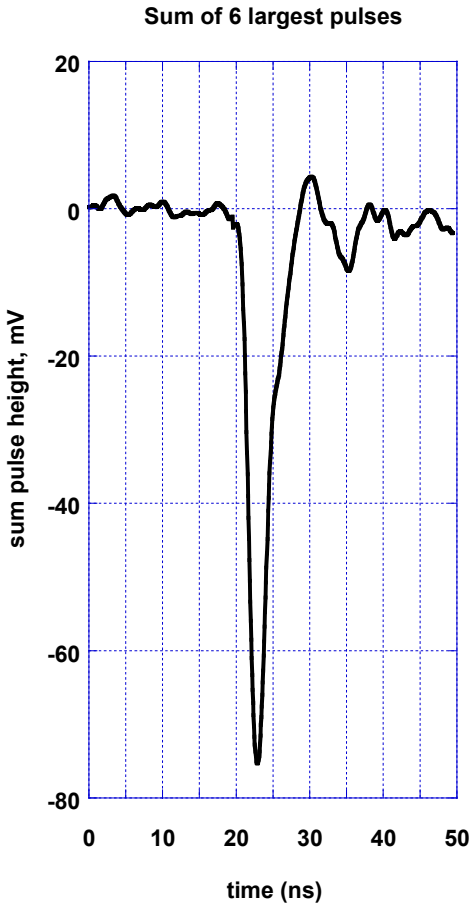

Figure 27. The sum of the 6 largest pulses giving an approximately noise-free shape, as the noise starts relatively small compared to each pulse and is then partially cancelled. The full width at half max is 3.0 ns, and is 8.3 ns at the base.

We can learn a bit more comparing **Figures 27** and **Figure 29,** which shows a pulse from a pulse generator set to have a rise time of 800 ps, and also shows the sum of 5 such pulses. The pulse generator output shown on the oscilloscope has a rise time of 1.5 ns, only slightly faster than the 1.6 ns of the Sr-90 pulses. This suggests that the Sr-90 pulses output from the 3D sensors may have rise times significantly faster than the observed 1.6 ns.

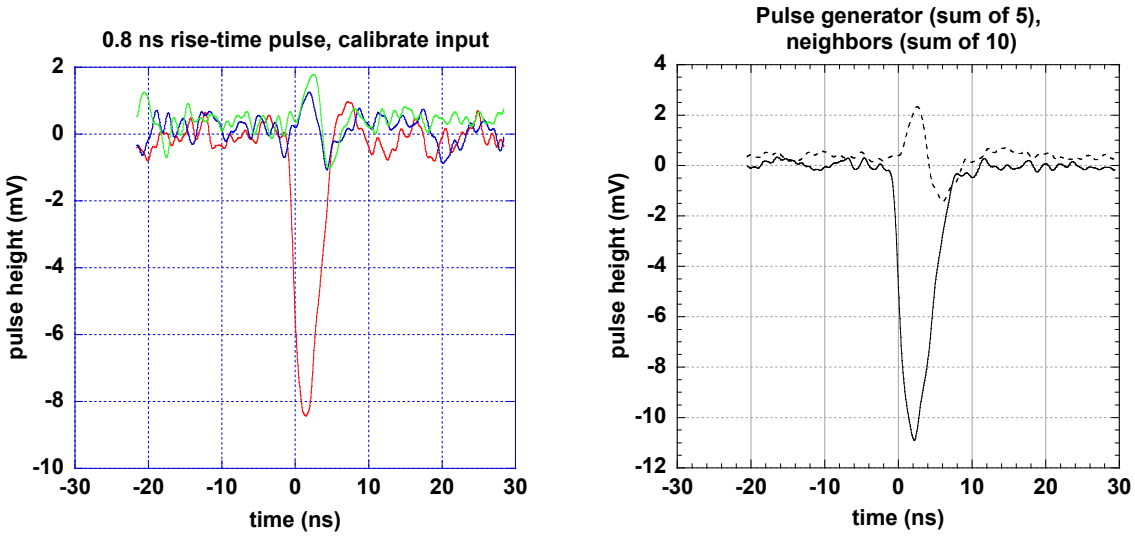

Figure 29. Pulses from an 800 ps rise-time pulse generator with the 2 neighboring channels (left), and the sum of 5 such pulses together with the sum of all 10 neighbor-channel pulses (right). The approximately noise-free shape shows no bulge on the trailing edge, indicating again the tail on the sensor pulses is not electronic in origin, but rather due to hole motion. It can also be seen that the signals in the neighboring channels are induced and that the noise is reduced.

The several ns wide bulge starting at 20% to 40% of the peak height on the trailing edges of the pulses in **Figures 17, 18, and 19** shows up quite clearly in **Figure 27**, is presumably due to the slower hole collection, and is not present in **Figure 29**, which shows pulse-generator pulses. The decrease of noise in **Figure 27** also shows up in **Figure 29** and the capacitative coupling of the pulse to the neighboring channels, which is visible in some of the earlier figures, is quite clear here.

The variation of the timing error with pulse height and signal-to-noise ratio in **Figure 30** is striking. The least-squares fit to a power-law of the time resolution, dt, vs. V, the pulse height, for the constant 50%-fraction method gives:

$$\mathbf{dt_{cf} = 581.4 / V^{0.9971}, R = 0.9993}$$

where dt is in ps, V is in mV, and R is the Pearson correlation coefficient.

For the fitting method:

$$\mathbf{dt_{fit} = 485.3 / V^{1.0171}, R = 0.99995}$$

The mean value of the 201 values at each pulse height is

$$\mathbf{dt_{mean} = 115.2 / V^{0.98655}, R = 0.99999.}$$

The dt from the constant fraction-50% method is about 20% - 23% larger than from the fitting method, reflecting the fact that the fitting method is not thrown off by a noise fluctuation at just one specific region (the pulse half-height in this case.) However, the

fitting method, using a more central 52, rather than the 67 signal points above, had errors that were several percent greater than the 50% constant fraction method.

The exponents are within 2% of a 45º slope, giving dt ≈ const. / V. This could be used when signals from multiple, sequential sensors are available, to give more weight to the low-noise-error, large pulses (from delta rays), so long as (1) the track is not one of the few that are very close to an electrode and (2) the last part of the pulse is not used for the fit – places where delta rays could cause pulse-shape errors. (These requirements are generally never satisfied by planar sensors.)

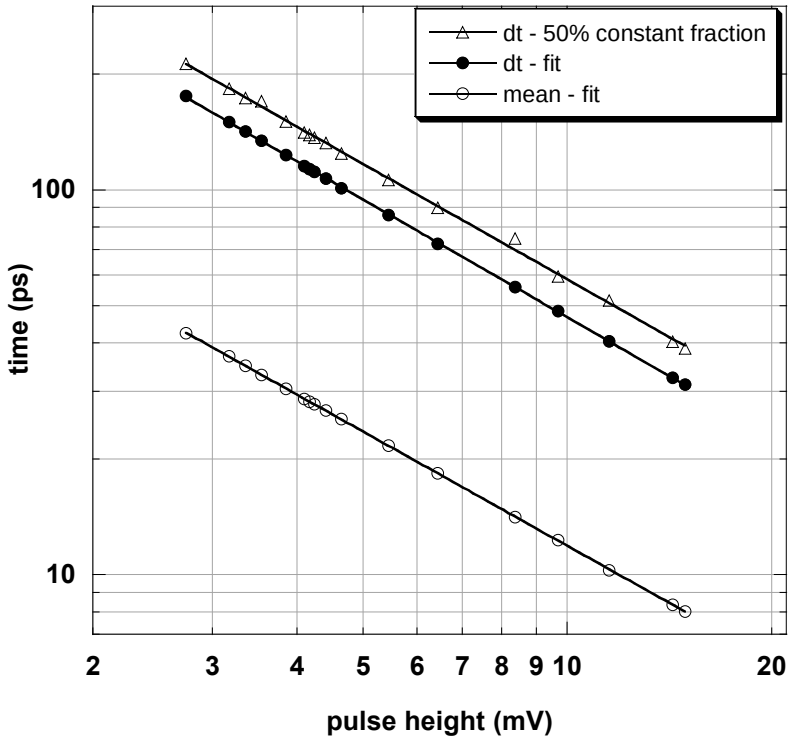

Figure 30. Expected time errors, dt, due to noise as a function of pulse height from the combined signal pulse shape added to 201 noise segments with dt determined from the standard deviation of time variation of the 50% point on the leading edge (Δ) and from the time variation of the best fit time of the combined signal pulse shape to the same shape plus noise (●). The mean value of the best fit times (○) is 24% of the fit values. The signal to noise ratio is 3 times the pulse height in mV.

The mean of the 201 standard deviations at each pulse height, while very small, in general would be expected to fluctuate above and below zero, rather that be consistently skewed toward later times as in **Figure 30**. This is due, in the parabolic interpolation of step 12 above, to (1) the use of more points ahead of the peak than after (to avoid the

need to simulate the fitting of hole tails such as the one seen in **Figure 27**), and (2) the more gentle slope after the peak. This combination causes a shift of the fitting pulse from the optimum time to one step early to tend to produce a larger error than from one step late, and the parabola responds by generally picking later times. **Figure 31** shows examples of such skewed distributions, one for a small pulse and one for a larger one.

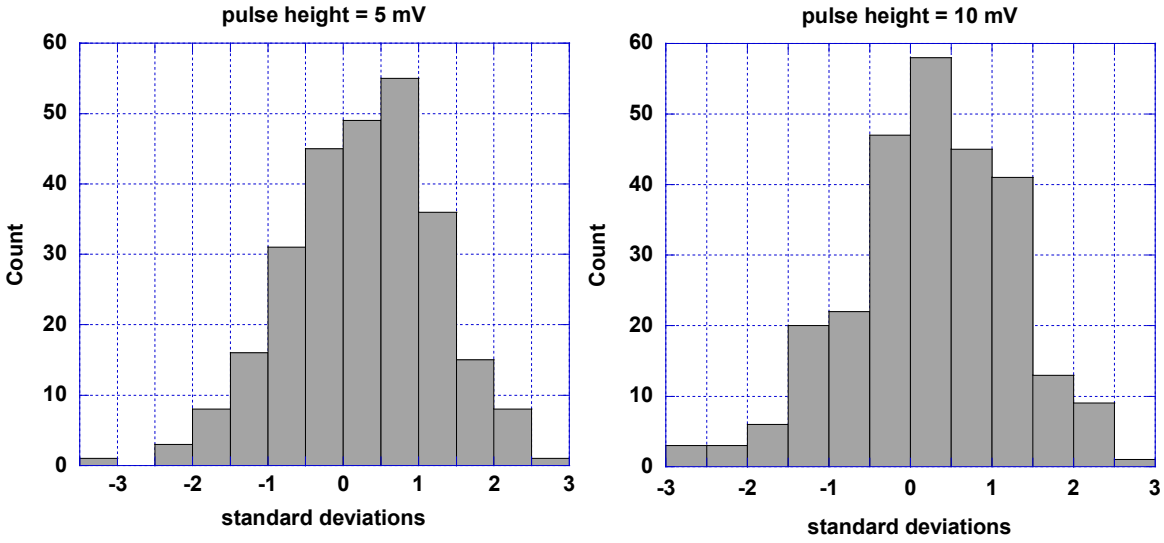

Figure 31. Distribution of standard deviations for a low and a high pulse height, showing the bias toward late values. Each standard deviation on the x-axis is equal to 94 ps for the 5 mV distribution and 46.9 ps for the 10 mV one.

While the fitting method could be adjusted for this effect, it would be an artificial one. After all, this data is just for a preliminary trial, to examine the effects of noise. The measurements used

- a large-capacitance sensor
- a beta source with the only collimation being the absence of a pulse in adjacent channels
- and employed no real knowledge of the track location.

It would be best to combine timing with tracking, predict the expected pulse shape, including the hole tail and fit the entire pulse. And this brings us to:

IX. NEXT

Before examining improvements to silicon technology we should examine the possibility of using diamond sensors. They could provide a modest improvement in performance.

One figure of merit is the charge generated per unit track length times the saturation velocity which gives the input current. Silicon, with more charge but a lower saturation velocity provides a net 35% more current for equal track lengths.

If noise is a limiting factor, and the signal size is proportional to q times v_{sat} divided by the sensor capacitance, C, for equal sizes, diamond becomes better by 57%. This would be reduced by the contribution of connection and circuit input capacitance. The net result could be a useful but limited advantage given the smaller industrial base for diamond, the greater cost, and other possible difficulties such as ones that might arise from the more than factor of two difference in coefficients of thermal expansion with a diamond pixel sensor and its readout chip. The improvements below apply the both silicon and to diamond.

There are many potential sources of major gains which are partially listed below. None of them have been used in this paper other than the intrinsic speed of 3D sensors, the fast current amplifier, and use of a waveform recorder (the oscilloscope). One item below, lowering capacitance by increasing the electrode separation of adjacent channels, will decrease the ratio of drift over peak electric fields and the constancy of the Ramo weighting field. Most of the others can be used simultaneously, given the conditions listed for each:

- reducing as far as practicable, the sensor capacitance,
- operation at reduced temperatures, with less noise and doubled speeds [29],
- use of an amplifier with the lowest possible noise, given the available space, heat removal capabilities, and speed requirements,
- use of higher electric fields giving drift velocities close to saturation values,
- use of trench-electrode sensors such as shown in **Figures 9** and **10,**
- use of waveform recorders if a channel can fit within the area of a pixel. Only the above-noise part of the signal is needed. One possibility is to determine the baseline by keeping track of its average as a single, updated number in storage.
- use of multiple timing layers of detectors, if allowed by Coulomb scattering, space, and cost considerations – some possibly rotated to help with tracking,
- use of a weighting factor, as suggested in section VIII, to favor layers having high signal-to-noise ratios,
- and, with similar limitations, use of high-resolution position-tracking layers (**The most accurate timing will be done by a system, not by one sensor – readout unit**.).

References

[1] Heijne, Erik, “Muon flux measurement with silicon detectors in the CERN neutrino beams” CERN-83-06, p. 18, 1983.

(2) K. Borer, A.G. Clark, R. Engelmann, 0. Gildemeister, C. Gössling, E. H. M. Heijne, P. Jarron, B. Lisowski, T. Pal, M. A. Parker and N. Redaelli, ”Construction and performance of a 1m^2 silicon detector in UA2”, *Nucl.Instr.and Meth.* A **253** (1987) 548-557.

[3] J. England, B. Hyams, L. Hubbeling, J. Vermeulen, P. Weilhammer, "Capacitative charge division read-out with a silicon strip detector", *Nucl. Instr. Meth.* **185** (1981) 43-47.

[4] J. Walker, S. I. Parker, B. Hyams, S. Shapiro, "Development of high density readout for silicon strip detectors", *Nucl. Instr. and Meth*. **226** (1984) 200-203.

[5] 13. C. Adolphsen, A. Litke, A. Schwarz, M. Turala, G. Anzivino, R. Horisberger, L. Hubbeling, B. Hyams, A. Breakstone, R. Cence, S. I. Parker, J. Walker, "Initial beam test results from a silicon-strip detector with VLSI readout", *IEEE Trans. on Nucl. Sci*., **33** (1986) 57-59.

[6] R. Sonnenblick, et al., "Electrostatic simulations for the design of silicon strip detectors and front-end electronics", *Nucl. Instr. and Meth.* A **310** (1991) 189.

[7] S. I. Parker, C. J. Kenney, and J. Segal, "3D--A proposed new architecture for solid-state radiation detectors", *Nucl. Instr. Meth*, **A395** (1997) 328-343.

[8] C. Kenney, S. Parker, J. Segal, and C. Storment, "Comparison of 3D and planar silicon detectors", *Proceedings of the 9th meeting of the Division of Particles and Fields of the American Physical Society*, Minneapolis, MN, 11-15 Aug 1996, World Scientific, 1998, **V2**, p1342-1345.

[9] C. Kenney, S. Parker, J. Segal, and C. Storment, "Silicon detectors with 3-D electrode arrays: fabrication and initial test results", *IEEE Trans. Nucl. Sci.* **46** (1999) 1224 – 1236.

[10] C. Kenney, S. Parker, B. Krieger, B. Ludewigt, T. Dubbs, and H. Sadrozinski, "Observation of Beta and X Rays with 3D-Architecture, Silicon Micro-Strip Sensors", *IEEE Trans. Nucl. Sci,* **48** (2001) 189 – 193.

[11] Sherwood I. Parker and Christopher J. Kenney, "Performance of 3-D architecture, silicon sensors after intense proton irradiation", *IEEE Trans. Nucl. Sci.,* **48** (Oct. 2001) 1629 - 1638.

[12] C. J. Kenney, S. I. Parker, and E. Walckiers, "Results from 3D sensors with wall electrodes: near-cell-edge sensitivity measurements as a preview of active-edge sensors", *IEEE Trans. Nucl. Sci,* **48** (2001) 2405 – 2410.

[13] J. Morse, C. Kenney, E. Westbrook, I. Naday, Sherwood Parker, "3dx: micromachined silicon crystallographic x-ray detector", *Proc. SPIE* **4784** (2002) 365-374.

[14] C. Da Via, "Radiation hard silicon detectors lead the way", *CERN Courier*, **43** (Jan. 2003) 23 – 26.

[15] C. Da Via, G. Anelli, J. Hasi, P. Jarron, C. Kenney, A. Kok, Sherwood Parker, E. Perozziello, S. J. Watts, "Advances in silicon detectors for particle tracking in extreme radiation environments", *Nucl. Instr. Meth.* **A 509** (2003) 86-91.

[16] J. Morse, C. Kenney, E. Westbrook, I. Naday, S. Parker, "The spatial and energy response of a 3d architecture silicon detector measured with a synchrotron X-ray microbeam", *Nucl. Instr. Meth.,* **A 524** (2004) 236-244.

[17] C. Da Via, J. Hasi, C. Kenney, A. Kok and S. Parker, "3D silicon detectors - status and applications", *Nucl. Instr. Meth*, **A549** (2005) 122-125.

[18] A. Kok, G. Anelli, C. Da Via, J. Hasi, P. Jarron, C. Kenney, J. Morse, Sherwood Parker, J. Segal, S. Watts and E. Westbrook, "3D detectors - state of the art", *Nucl. Instr. Meth*. **A560** (2006) 127-130.

[19] C. J. Kenney, J. D. Segal, E. Westbrook, Sherwood. Parker, J. Hasi, C. Da Via, S. Watts, J. Morse, "Active-edge planar radiation sensors", *Nucl. Instr. Meth*, **A565** (2006) 272-277.

[20] S. Parker, C. J. Kenney, D. Gnani, A. C. Thompson, E. Mandelli, G. Meddeler, J. Hasi, J. Morse, E. M. Westbrook, "3DX: an X-ray pixel array detector with active edges", *IEEE Trans. Nucl. Sci.,* **53** (2006) 1676-1688.

[21] C.J. Kenney, J. Hasi, Sherwood Parker, A. C. Thompson, E. Westbrook, "Use of active-edge silicon detectors as X-ray beam monitors", *Nucl. Instr. Meth*, **A582** (2007) 178-181.

[22] C. Da Via, J. Hasi, C. Kenney, V. Linhart, S. Parker, T. Slavicek, S.J. Watts, P. Bem, T. Horazdovsk, S. Pospisil, "Radiation hardness properties of full-3D active edge silicon sensors", *Nucl. Instr. Meth*, **A587** (2008) 243-249.

[23] Cinzia Da Via, Sherwood Parker, Mario Deile, Thor-Erik Hansen, Jasmine Hasi, Christopher Kenney, Angela Kok, Stephen Watts, "Dual Readout – Strip / Pixel Systems", *Nucl. Instr. Meth* **A594** (2008) 7.

[24] Sherwood Parker, Cinzia Da Via, Mario Deile, Thor-Erik Hansen, Jasmine Hasi, Christopher Kenney, Angela Kok, Stephen Watts, Dual Readout, "3D Direct / Induced-Signals Pixel Systems", *Nucl. Instr. Meth* **A594** (2008) 332.

[25] M. Mathes, M. Cristinziani, C. Da Via', M. Garcia-Sciveres, K. Einsweiler, J. Hasi, C. Kenney, Sherwood Parker, L. Reuen, M. Ruspa, J. Velthuis, S. Watts, N. Wermes, "Test Beam Characterization of 3-D Silicon Pixel Detectors", *IEEE Trans. Nucl. Sci.,* **55** (2008) 3731.

[26] Cinzia Da Vià*, Mario Deile*, Jasmine Hasi, Christopher Kenney, Angela Kok, Sherwood Parker*, Stephen Watts, et al., "3D Active Edge Silicon Detector Tests with 120 GeV Muons", *IEEE Trans. Nucl. Sci.* **56** (2009) 505.

[27] C. Da Viá, E. Bolle, K. Einsweiler, M. Garcia-Sciveres, J. Hasi, C. Kenney, V. Linhart, Sherwood Parker, S. Pospisil, O. Rohne, T. Slavicek, S. Watts, N. Wermes, "3D Active Edge Silicon Sensors with Different Electrode Configurations: Radiation Hardness and Noise Performance", *Nucl. Instr. Meth* **A604** (2009) 505–511.

[28] P. Jarron, et al., "A transimpedance amplifier using a novel current mode feedback loop", *Nucl. Instr. Meth* A 377 (1996) 435.

[29} G. Anelli, et al., "Noise characterization of a 0.25 μm CMOS technology for the LHC experiments", *Nucl. Instr. Meth* A 457 (2001) 361.

[30] G. Anelli, et al., "A high-speed low-noise transimpedance amplifier in a 0.25 μm CMOS technology", *Nucl. Instr. Meth* A 512 (2003) 117.

[31] Simon Ramo, "Currents Induced by Electron Motion", *Proceedings of the I.R.E.*, **27** (1939) 584.

[32] W. Shockley, "Currents to Conductors Induced by a Moving Point Charge", *Journal of Applied Physics*, **9** (1938) 635.

[33] G. Cavalleri, E. Gatti, G. Fabri, and V. Svelto, " Extension Of Ramo's Theorem As Applied To Induced Charge In Semiconductor Detectors", *Nuclear Instruments and Methods* **92** (I97I) I37

[34] Particle Data Group, "Particle physics booklet", pp 217 – 221, July 2008, or C. Amsler, et al., "Review of Particle Physics", *Physics Letters* **B 667** (2008) 1. Delta ray production rate formulas are given in many references, but some older ones are both difficult to find and may assume the velocity of the incident particle is not close to c. This reference is also available at **http://pdg.lbl.gov/**.

[35] Alexandre Real Couture, Dominique Drouin, Raynauld Gauvin, **"**CASINO V2.42 - A Fast and Easy-to-use Modeling Tool for Scanning Electron Microscopy and Microanalysis Users". (A user's manual of the version of CASINO used here is published in the journal *Scanning*, Volume 29, Issue 3 **,** 2007, Pages 92 – 101.)

[36] C. Jacoboni, C. Canali, G. Otiaviani and A. Alberigi Quaranta, "A review of some charge transport properties of silicon", *Solid-State Electronics*, **20** (1977) 77-89.

[37] F. Nava, C. Canali, and L. Reggiani, "On the diffusivity of holes in silicon*", J. Appl. Phys.* **50** (1979) 922.

[38] S. O. Rice, "Mathematical analysis of random noise, Part III: Statistical properties of random noise currents", Bell System Technical Journal 24 (1945) 55, equation (3.3 – 13).

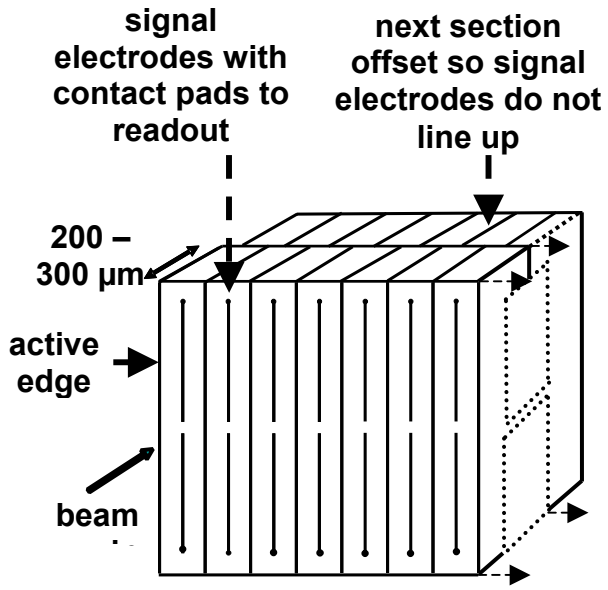

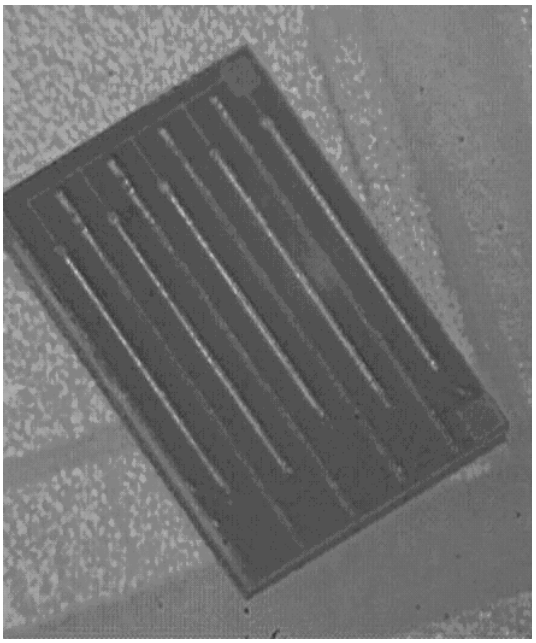

Figure 9. Schematic diagram of part of one section of two of the planes in an active-edge 3D trench-electrode detector. Other offsets (⅓, ⅔, 0, ⅓, ⅔ ..etc.) may also be used.